Carbon Emcoating Architecture Boosts Lithium Storage of Nb_2O_5

Qing Ji[1,2†], Zhuijun Xu[1,3†], Xiangwen Gao[4,5†], Ya-Jun Cheng[1,4*], Xiaoyan Wang[1], Xiuxia Zuo[1], George Z. Chen[2, 6], Binjie Hu[2*], Jin Zhu[1], Peter G. Bruce[4,7,8], Yonggao Xia[1, 9*]

1. Ningbo Institute of Materials Technology and Engineering, Chinese Academy of Sciences, 1219 Zhongguan West Road, Zhenhai District, Ningbo, Zhejiang Province 315201, People's Republic of China

2. The University of Nottingham Ningbo China, 199 Taikang East Road, Ningbo, Zhejiang Province 315100, People's Republic of China

3. University of Chinese Academy of Sciences, 19A Yuquan Rd, Shijingshan District, Beijing 100049, People's Republic of China

4. Department of Materials, University of Oxford, Parks Rd, OX1 3PH, Oxford, United Kingdom

5. Materials Science and Engineering Program and Texas Materials Institute, University of Texas at Austin, Austin, TX 78712, USA

6. University of Nottingham, University Park, Nottingham NG7 2RD, United Kingdom

7. The Henry Royce Institute, Parks Road, Oxford OX1 3PH, United Kingdom.

8. The Faraday Institution, Quad One, Becquerel Avenue, Harwell Campus, Didcot OX11 OR1, United Kingdom

9. Center of Materials Science and Optoelectronics Engineering， University of Chinese Academy of Sciences, 19A Yuquan Rd, Shijingshan District, Beijing 100049, P. R. China

AUTHOR INFORMATION

*Corresponding Author

E-mail Address: chengyj@nimte.ac.cn, binjie.hu@nottingham.edu.cn, xiayg@nimte.ac.cn

†These authors contributed equally to this work.

ABSTRACT

Intercalation transition metal oxides (ITMO) have garnered great attention as lithium-ion battery negative electrodes due to good operation safety, high capacity and rapid ion intercalation. However, the intrinsic low electron conductivity plagues the lifetime and cell performance of ITMO negative electrode. Here we design a new carbon-emcoating architecture through single CO_2 activation treatment as demonstrated by the Nb_2O_5/C nanohybrid. Triple structure engineering of the carbon-emcoating Nb_2O_5/C nanohybrid is achieved in terms of porosity, composition, and crystallographic phase. Superior cycling and rate performance are delivered compared to the conventional carbon coating and carbon embedding Nb_2O_5/C nanohybrids. Reversible capacity of 387 mAh g^{-1} is shown at 0.2 C and 92 % of capacity is retained after 500 cycles at 1 C. Differential electrochemical mass spectrometry (DEMS) indicates that the carbon emcoated Nb_2O_5 nanohybrids presents less gas evolution than commercial lithium titanate oxide during cycling. The unique carbon emcoating technique can be universally applied to other ITMO negative electrodes to achieve excellent electrochemical performance.

KEYWORDS

Niobium Pentoxide/carbon nanohybrids; Mesoporous; CO_2 activation; Emcoating; Lithium-Ion Battery Negative Electrode

INTRODUCTION

With high theoretical capacity, high redox potential, and low volume change, intercalation transition metal oxides (ITMO) appeal to researchers as alternatives for lithium-ion battery negative electrodes[1, 2]. However, intrinsic low electric conductivity restricts the rate performance and further practical application of the ITMO. Great efforts on constructing nanostructured ITMO have proved that size reduction is an effective method to shorten the Li-ion diffusion length and offer better accessibility for the electrolyte[3]. However, the low electron conductivity issue remains. Compositing nanostructured-ITMO with carbon matrix is a promising strategy to achieve enhanced rate performance and the carbon matrix stabilizes the ITMO nanoscale structure simultaneously during lithium ion insertion/extraction[4]. In general, carbon coating and carbon embedding are two conventional strategies to integrate the ITMO with carbon[5-10]. However, the typical carbon coating tends to proceed only on the outer surface of the ITMO because the carbon source finds it difficult to access the interior region of the agglomerate. Methods such as core-shell structure construction allow enhanced carbon coating; however, convoluted process is normally involved[5]. Besides, the core-shell structure still retains individual nanoparticulate feature, which could bring adverse effects such as inferior tap density[11]. Compared to the coating method, the carbon embedding offers continuous carbon wrapping on the total surface of the ITMO[10, 12, 13]. Micro-/nano scale hierarchical architectures can be built based on the embedding method. As a result, side effects originated from the nano-sized structure feature can be circumvented[14].

Our group has developed a new concept to embed nanoscale ITMO (NbO_2, Nb_2O_5, TiO_2 and $Li_4Ti_5O_{12}$) in the carbon matrix using dimethacrylate based dental resin monomer as the solvent and carbon source over the past few years[15-19]. Metal ions are incorporated into polymer network during curing process where the dental resin monomer reacts with the ITMO precursors. Thus, super-small metal oxide nanoparticles are *in situ* generated and embedded in the carbon matrix homogeneously during the carbonization process. The as-prepared metal oxide/carbon nanohybrids present high tap density and unique electrochemical performance. However, a few critical issues remain. High content of dense structured carbon prevents the wetting of the electrolyte to access the ITMO within the carbon matrix, where electrochemical kinetics is retarded, and apparent electrochemical performance is compromised. Besides, excessive carbon matrix is generated surrounding the ITMO nanoparticle, which makes significant contribution to the overall capacity while the intrinsic ITMO electrochemical performance is smeared[20-22]. Furthermore, the *in situ* formed carbon matrix suppresses the growth of metal oxide nanocrystal, which yields poor crystallinity and short lithiation plateau. As a result, the characteristic lithiation/delithiation profiles are deviated and the complexity of battery management is increased in practical applications.

Here, a unique emcoating concept is developed to perform carbon compositing with the nanostructured ITMO, which combines the advantages of both coating and embedding methods, while the drawbacks are avoided. Carbon emcoated Nb_2O_5 nanohybrids are constructed through a facile scalable one-step carbon dioxide (CO_2)

activation of the Nb_2O_5/C nanohybrid with the embedding structure feature. Triple structure engineering including carbon content modification, porosity tuning, and crystallographic phase manipulation of the Nb_2O_5/C emcoating nanohybrid is achieved. This strategy possesses several distinct advantages. Firstly, excessive carbon is etched, and thin carbon coating is formed on the surface of each individual Nb_2O_5 nanoparticle, while the continuous electron conductive network remains. The shortened pathway from electrolyte to the Nb_2O_5 nanoparticle enables accelerated lithium ion diffusion, leading to enhanced electrochemical kinetics and improved rate performance. Secondly, the Nb_2O_5 nanoparticles are still homogeneously distributed within the micrometer-scale continuous conductive carbon matrix inherited from embedding structure. The agglomeration of the Nb_2O_5 nanoparticles is suppressed, where individual Nb_2O_5 nanoparticles can effectively participate in the lithiation process. Besides, the homogeneous dispersion of the Nb_2O_5 nanoparticles within the carbon matrix helps to relief mechanical stress upon lithiation, leading to improved cyclic stability. Thirdly, compared with conventional activation methods such as hot air and KOH treatments, CO_2 activation is regarded as mild, controllable, facile, free of post-treatment, and easy to scale-up, which is particularly attractive for practical applications. Consequently, the construction of the emcoating structure within the Nb_2O_5/C nanohybrid endows excellent cycling stability and rate capability. Comprehensive studies on fundamental mechanism for emcoating structure construction, phase transition of Nb_2O_5 during structure evolution, and structure-property correlation of the Nb_2O_5/C emcoating nanohybrid are carried out in this work.

RESULTS AND DISCUSSIONS

Figure 1 schematically illustrates the structural evolution from embedding to emcoating of the Nb_2O_5/carbon nanohybrids through the CO_2 activation process[23, 24]. The Nb_2O_5 nanoparticles of the pristine sample are fully embedded in the dense carbon matrix. With CO_2 activation, the dense carbon matrix is partially etched first, while the spatial distribution state of the Nb_2O_5 nanoparticles remains intact. CO_2 only etches the surface of carbon matrix; the inner carbon keeps its dense structure, and this carbon composition state is noted as Nb_2O_5 emcoated with dense carbon (Emcoating with Dense Carbon, abbreviated as EDC). With further CO_2 activation, the outer surface of the Nb_2O_5 particles has no carbon coating anymore (defined as exterior region). However, the inner carbon matrix is only partially etched and thin coating layer is retained on the inner surface of the Nb_2O_5 particles (defined as interior region). This thin carbon coating on the inner surface of each Nb_2O_5 particles is connected and continuous carbon network is therefore preserved. The thin carbon coating layer tends to be porous because of extensive CO_2 activation. Thus, the sample presenting emcoating structure with thin, porous and interconnected carbon coating is fabricated (Emcoating with Porous Carbon, abbreviated as EPC).

From a structure model perspective, both the EDC and EPC structures can be defined as following:

EDC: Full carbon coating particles inter-connected by dense carbon matrix. Within this structure, any two arbitrary points at the surface of the Nb_2O_5 particle can be connected by at least one route throughout the carbon matrix. In actual material systems,

tremendous amount of points at the particle surface are connected by at least one route throughout the carbon matrix. The particles are fully covered by carbon, which are further connected by carbon matrix. Because the carbon matrix is not etched, it remains a dense structure.

EPC: Partial carbon coating particles inter-connected by porous carbon matrix. In actual material systems, the carbon coating at the surface of the particles is partially removed, leaving part of the particle surface naked. Meanwhile, the carbon matrix inter-connecting neighbouring particles becomes porous due to partial carbon removal.

Exterior region of the EPC: Carbon free region on the surface of the particles within the EPC. Inside this specific region, any two arbitrary points at the surface of the Nb_2O_5 particles cannot be connected by a route throughout the carbon matrix. In actual material systems, this region may have some small areas still covered by residual carbon. However, it is generally defined as the exterior region of the EPC for the reason of simplicity.

Interior region of the EPC: Carbon remaining region within the EPC. In this specific region, there are at least two points at the surface of the Nb_2O_5 particles connected by at least one route throughout the carbon matrix. However, in actual material systems, tremendous amount of points is connected by at least one route throughout the carbon matrix.

Compared with the pristine embedding structure, the emcoating structure bears a good conductivity with less carbon content. Additionally, the EPC structured Nb_2O_5/C nanohybrid provides enhanced accessibility towards electrolyte and shortened Li-ion

transportation path for Nb_2O_5 nanoparticles than the EDC structure as interpreted by the sketch in **Figure 1**.

Coral structured Nb_2O_5 will be generated by further enhanced CO_2 activation with extended time or elevated temperature (for example, at 900 ˚C), where carbon matrix is fully eliminated, and naked Nb_2O_5 nanoparticles come to agglomerate. Carbon coating can be further made onto the coral Nb_2O_5 by different methods such as chemical vapor deposition (CVD) and mechanical ball-milling. However, the carbon coating can only proceed at the outer surface of the coral structured Nb_2O_5, where the interior region is difficult to be coated. It is impossible to build the emcoating structure via CO_2 activation treatment of the carbon coated coral Nb_2O_5 particulate agglomerate. Electron conductivity improvement from carbon coating is not as efficient as from the emcoating structure.

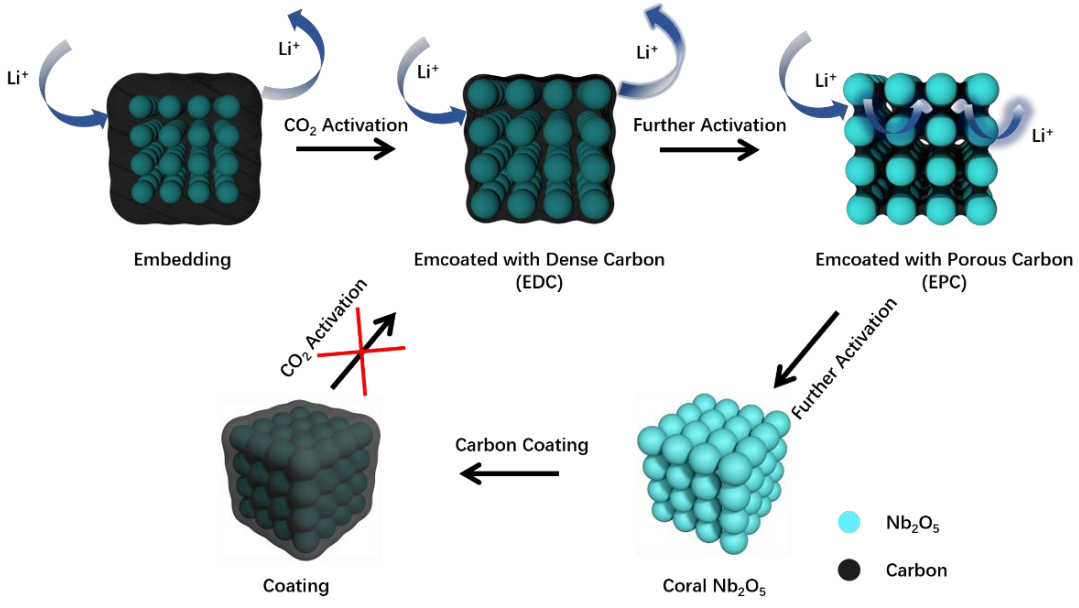

Figure 1. Schematic illustration of structure evolution of the Nb_2O_5/carbon nanohybrids from embedding to emcoating.

The actual structure evolution of the Nb_2O_5/C nanohybrid from embedding to emcoating induced by CO_2 activation is characterized by SEM and TEM (**Figure 2** and **Figure S1**). The pristine carbon embedded Nb_2O_5 nanohybrid presents a dense bulk structure with a smooth surface, particle size ranging from 1 μm to 5 μm (**Figure 2a-1**). Upon CO_2 activation at 800 ˚C, the Nb_2O_5 nanoparticles grow from 5 nm (**Figure 2a-2**) to 20 - 50 nm (**Figure 2b-2**). HRTEM and SAED image shows a clear phase transition from hexagonal phase in the pristine (**Figure 2a-3** and **2a-4**) to the orthorhombic phase (**Figure 2b-3** and **2b-4**). The surface of the EDC structured Nb_2O_5/C nanohybrid becomes porous and rough with some nanoparticles exposed at the surface due to consumption of carbon by CO_2 (**Figure 2b-1**). It proves that only slight surface activation occurs at 800 °C, consistent with previously reported work[25-28]. After further treatment at 900 ˚C, small pores are generated at the surface of the EPC structured Nb_2O_5 (**Figure 2c-1**). A bimodal particle size distribution is observed with the EPC structured Nb_2O_5, which are 15 nm - 20 nm and 50 nm - 100 nm respectively (**Figure 2c-2**). HRTEM (**Figure 2c-3** and **2c-4**) confirms the small crystal refers to the orthorhombic Nb_2O_5 and the large one refers to the monoclinic Nb_2O_5. In addition, the EPC sample shows more porous structure inside the carbon matrix, consistent with the surface morphology revealed by the SEM images. With further activation time, coral structured Nb_2O_5 is presented **(Figure S1 a-1**). The grain size grows to 100 nm and the crystallographic phase is fully transferred to the monoclinic Nb_2O_5 (**Figure S1b**), confirmed by the diffraction patterns from the SAED result. The microscopic structure characterization illustrates that the carbon matrix evolves from

dense bulk to porous and interconnected structure due to CO_2 activation, while the spatial distribution of the Nb_2O_5 nanoparticles remain intact within the carbon matrix.

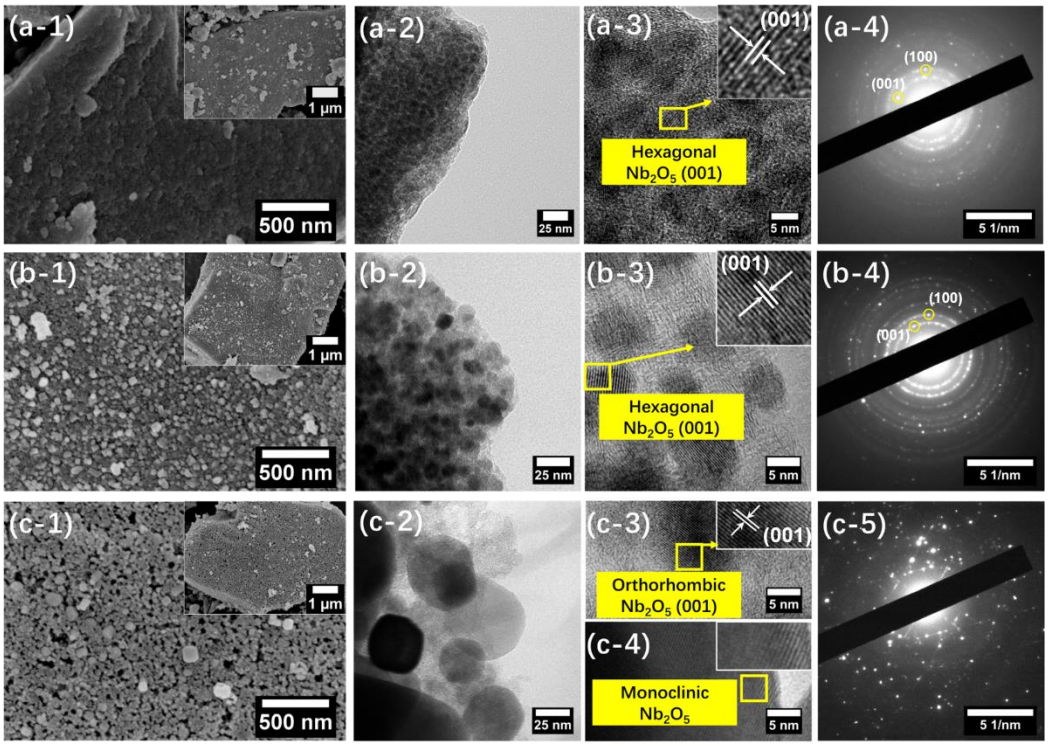

Figure 2. Structure evolution of the Nb_2O_5/C nanohybrid from pristine Nb_2O_5 embedded with carbon (image a series) to emcoated with dense carbon (EDC, activated at 800 ˚C for 2 h, image b series), and to emcoated with porous carbon (EPC, activated at 900 ˚C for 1 h, image c series) induced by the CO_2 activation. Image details: SEM (a-1, b-1, and c-1), TEM (a-2, b-2, and c-2), HRTEM (a-3, b-3, c-3, and c-4), and SAED (a-4, b-4, and c-5). Insets in a-1, b-1, and c-1: low magnification SEM images of the Nb_2O_5/C nanohybrids.

To further gain insights about the interior carbon distribution of the emcoating structure, a simulation model is established to estimate surface area contribution proportion from different regions of the Nb_2O_5 nanoparticulate agglomerate (**Figure 3**).

Based on the actual size revealed by the microscopic images, the nanoparticulate agglomerate is approximated as a cube with a length of 5.5 μm, built by packing the nanoparticles with a diameter of 7.8 nm. The simulation model demonstrates that the inner surface provided by the particles contributes more than 99.7 % of the total surface area; while the outer surface area accounts only 0.3 % of the total surface area. The simulation results suggest that the emcoating strategy enables carbon coating on the majority of the surface area of the nanoparticulate agglomerate. While the conventional carbon coating can only coat the outer surface area, which is only a tiny portion of the total surface area. Compared to the conventional surface coating method, the emcoating strategy holds a great potential to improve electrochemical kinetics and rate capability by coating carbon onto the inner surface of the nanoparticulate agglomerate.

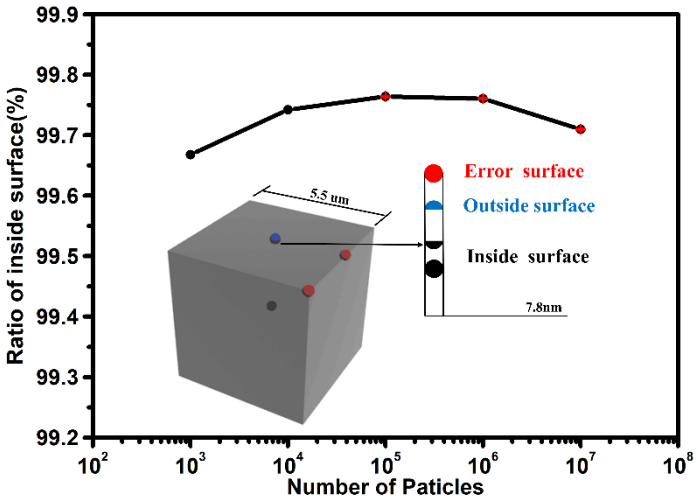

Figure 3. Simulation model of the nanoparticulate powder for inner and outer surface area distribution estimation. Grey Cube: bulk shape of the Nb_2O_5 nanoparticulate agglomerate. Black Sphere: Inside part of the Nb_2O_5 particles. Blue Sphere: Outside part of the Nb_2O_5 particles. Red Sphere: Nb_2O_5 particles on the edge of cube.

Carbon contents of the Nb_2O_5/C nanohybrids are determined by TGA. **Figure 4a** and **S2a** indicate that the carbon content decreases when the structure changes from embedding to emcoating after the CO_2 activation. In addition, both increasing activation temperature and elongated activation time reduce the carbon content: the carbon etching process at 900 ˚C is much stronger than that at 800 ˚C and the carbon component is fully removed when the sample is processed at 900 ˚C for 2 hours. To be precise, the pristine embedding type Nb_2O_5/C nanohybrid presents the carbon content of 40 %, while the carbon contents of the EDC, EPC and coral Nb_2O_5 are 27 %, 8 % and 0 %, respectively (**Table S1)**. Both the pristine and CO_2 activated samples present characteristic peaks of disordered carbon (D-band) at 1360 cm^{-1} and graphitic carbon (G-band) at 1590 cm^{-1} in the Raman spectra, **Figure 4b**. Although the coral structured Nb_2O_5 display no carbon content from the TGA result, trace amount of carbon contributes to the characteristic peaks, **Figure S2b**. The integrative intensity ratio of the D band and the G band (I_D/I_G) refers to the extent of disordered carbon (**Table S1**). The I_D/I_G value decreases with increasing activation temperature, which indicates higher graphitization after activation[29, 30]. In addition, with activation under 900 ˚C, small peaks appear at fingerprints region, and the coral structured Nb_2O_5 bears strong peaks at 118 cm^{-1}, 261 cm^{-1}, 632 cm^{-1}, and 992 cm^{-1} originated from the Nb_2O_5 phase[31]. The increasing peak intensity of the Nb_2O_5 is assigned to the particle growth and enhanced crystallization, consistent with the TEM images[32].

Brunauer-Emmett-Teller (BET) measurements investigate the porosity evolution of the Nb_2O_5/C nanohybrids along with different CO_2 activation treatments (**Figure 4c-4f**). The pristine carbon embedding Nb_2O_5 presents type I adsorption/desorption isotherms, referring to a microporous structure (**Figure 4c**). After CO_2 activation, typical type IV isotherms are observed in the EDC and EPC structured Nb_2O_5, and the pore size distribution shifts to 3.8 nm (EPC structured Nb_2O_5) and 20 nm (EDC structured Nb_2O_5), confirming the presence of mesoporous structure (**Figure 4d** and **4e**)[33]. Note that CO_2 activation would generate micropores on the surface of carbon matrix, thus slight pore size increase is detected[25, 26]. The coral Nb_2O_5 possesses the type II isotherms with a non-porous structure (**Figure S2d**). As the porous structure is mostly contributed by the carbon content in the nanohybrid, the pores vanish due to full removal of the carbon component by CO_2. Assisted by the strong pore generation effect of CO_2 activation under 900 ˚C, the EPC structured Nb_2O_5 presents a substantial increase of BET surface area from 57.7 m^2g^{-1} to 221 m^2g^{-1} (**Table S2**). While the EDC structured Nb_2O_5 shows only a minor increase of the surface area due to less extent of the CO_2 activation at a low temperature.

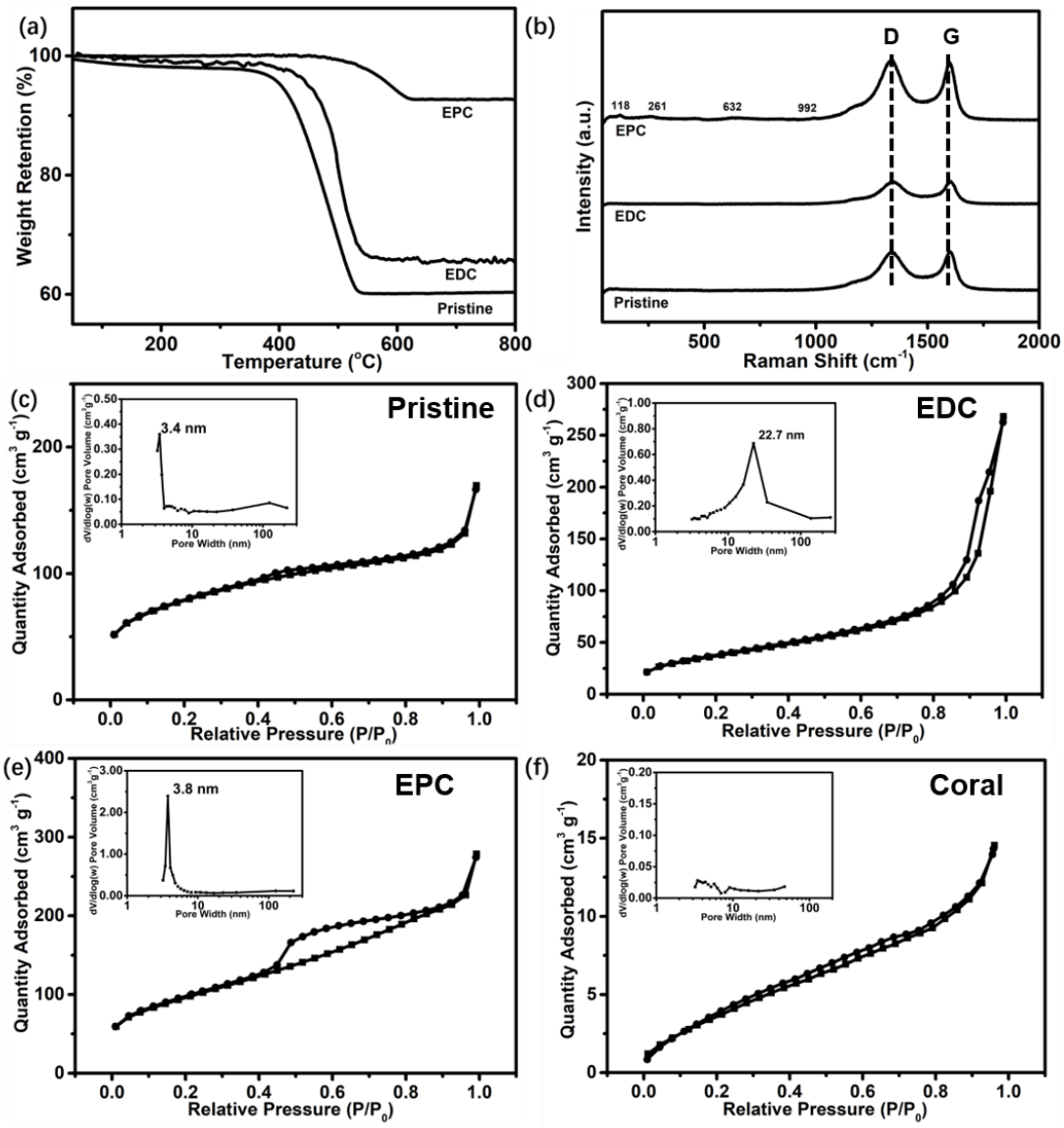

Figure 4. Structure characterizations of the Nb_2O_5/C nanohybrids with carbon embedding (pristine), emcoating with dense carbon (EDC), and emcoating with porous carbon (EPC). Thermogravimetric profiles (a) and Raman spectroscopy (b) of the pristine, embedded, and emcoated Nb_2O_5; N_2 adsorption/desorption isotherms (Inset: corresponding BJH pores size distribution curves) of the pristine embedded Nb_2O_5 (c), EDC structured Nb_2O_5/C (d), EPC structured Nb_2O_5/C (e) and coral Nb_2O_5 (f).

XRD is applied to investigate the crystallographic phase change of the Nb_2O_5/C nanohybrids induced by the CO_2 activation (**Figure 5a** and **5b**). Compared to the pristine carbon embedding Nb_2O_5/C nanohybrid, the diffraction peaks of both the EDC and EPC samples become sharper, showing enhanced crystallization of the Nb_2O_5 nanoparticles through the CO_2 activation process, consistent with the TEM results. In addition, different crystallographic phases are observed with the CO_2 activation at 800 °C and 900 °C. The pristine carbon embedding Nb_2O_5/C nanohybrid presents a typical hexagonal phase (JCPDS No. 28-0317) (**Figure 5a**); while the EDC structured Nb_2O_5/C shows a splitting peak at 28 °, implying a transformation from hexagonal phase to orthorhombic phase (JCPDS No. 27-1003). When the activation temperature increases to 900 °C, the EPC structured Nb_2O_5/C presents further phase transition from pure hexagonal phase to bi-phase of orthorhombic/monoclinic (**Figure 5b**) with the quantities of the orthorhombic and monoclinic of 43.1% and 56.9 %, respectively, based on a reference intensity ratio (RIR) method[34]. Generally, the phase transition of Nb_2O_5 from hexagonal to monoclinic depends on the annealing temperature (**Table 1**). Although the pristine sample is synthesized at 900 °C, the dense-structured carbon matrix can introduce carbon doping into the Nb_2O_5 nanoparticles, which hinders the phase transition from hexagonal to orthorhombic/monoclinic under 900 °C. Such obstruction effect by the doped carbon has been revealed in the TiO_2 phase transition[35-38]. During the CO_2 activation process, the carbon matrix is etched gradually, which partially eliminates the doped carbon and facilitates phase transition.

In order to understand mechanism governing the phase transition of Nb_2O_5 induced by the CO_2 activation, XPS is applied to detect the valence state and chemical environment of the Nb_2O_5 nanoparticles. The XPS spectra (**Figure 5d-5f** and **Figure S3**) confirm the existence of carbon, oxide and niobium on the surface of the Nb_2O_5/C nanohybrid. Peaks assigned to the binding energies of 287.5 eV and 288.5eV are observed in the high resolution C1s XPS spectra, which are originated from the carbonate species[39, 40]. The existence of these peaks indicates that the Nb_2O_5 nanoparticles are doped by C^{4+}. Apart from the C1s spectra, the O1s spectra present a peak located at around 532 eV, which is ascribed to the carbonate species as well[41]. **Table S3** shows that the pristine embedding Nb_2O_5/C nanohybrid presents the highest content of carbonate species, which inhibits the phase transition of the Nb_2O_5 nanoparticle. Thus, the phase transition is precluded at 900 ˚C and the Nb_2O_5 nanoparticles remain as hexagonal phase. With carbon consumption through the CO_2 activation process, the amount of the carbonate species decreases as indicated by the XPS spectra. The restriction effect of the carbon doping on the phase transition is weakened, where the phase transition from hexagonal to orthorhombic and monoclinic is observed.

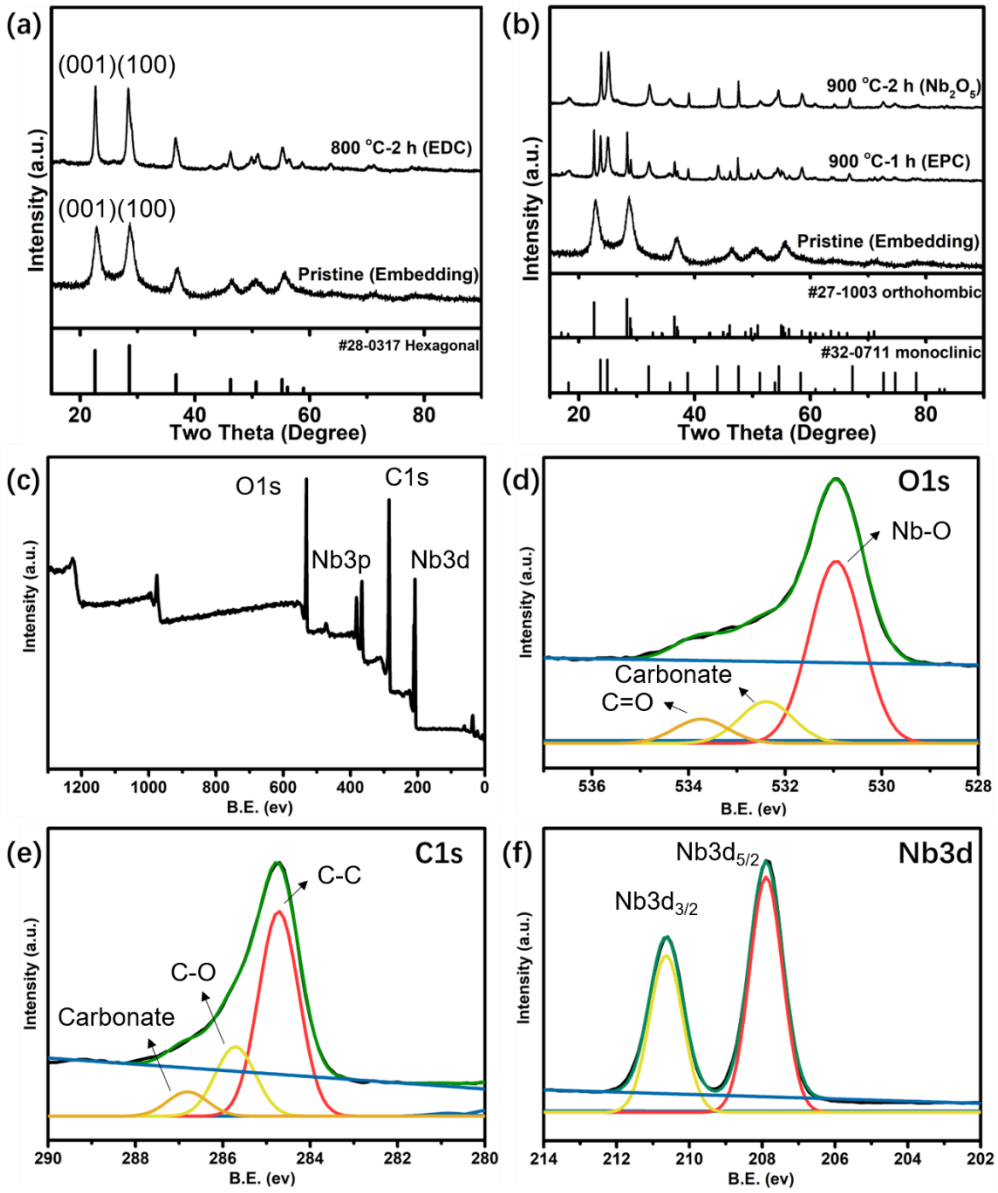

Figure 5. XRD patterns of pristine carbon embedded Nb_2O_5/C and carbon emcoated (both EDC and EPC) Nb_2O_5/C nanohybrids (a and b). XPS survey (c) and high resolution O1s (d), C1s (e) and Nb3d (f) of the EPC structured Nb_2O_5/C nanohybrid.

Table 1. Relationship between heat-treatment temperature and crystallographic phase of Nb_2O_5[42]

Temperature (˚C)	Crystallographic phase
500-600	Hexagonal
600-800	Orthorhombic
900	Monoclinic

Based on the comprehensive structure analysis of the Nb_2O_5/carbon nanohybrids, the mechanism of the phase transition induced by the CO_2 activation process is interpreted. The hexagonal phase of Nb_2O_5 is normally only stable in the temperature range from 500 ˚C to 600 ˚C, while phase transition tends to occur at elevated temperatures[42, 43]. However, the existence of dense carbon coating and carbon doping precludes the phase transition and the hexagonal phase is retained at 900 ˚C in this work. When activated by CO_2, the carbon species is etched, alleviating the mechanical stress and reducing the amount of the doped carbon simultaneously. As a result, the energy barrier for the phase transition is lowered, where transition from hexagonal to orthorhombic and monoclinic phase occurs[44]. The phase transition from the hexagonal phase to the orthorhombic and further monoclinic phase is triggered with either extended time range or elevated temperature of the CO_2 activation treatment.

It is noted that, according to our previous work, Nb_2O_5 would be reduced to NbO_2 through equation 1 and 2, which was generated from the residual amount of CO_2 in the tube furnace[18]. While, in this work, under CO_2 atmosphere, the abundant CO_2 pushed the reaction of equation-2 towards the left direction. Thus, Nb_2O_5 will not be reduced to NbO_2.

$$CO_2 + C \rightarrow 2CO \quad (1)$$

$$CO + Nb_2O_5 \leftrightarrow 2NbO_2 + CO_2 \quad (2)$$

The electrochemical performance of the CO_2 activated Nb_2O_5/C nanohybrids are tested using CR-2032 coin type half-cells. **Figure 6a** and **Figure S4** exhibit the cyclic voltammetry (CV) curves of the activated samples at 0.2 mV s^{-1} with voltage range

from 0.005 V to 3.0 V. No obvious redox peak is observed in pristine carbon embedding Nb_2O_5/C nanohybrid due to the poor crystallization of the Nb_2O_5 component. After CO_2 activation, the EDC structured Nb_2O_5/C nanohybrid shows redox couple of Nb^{4+}/Nb^{5+} at 1.84 V/1.62 V, referring to the delithiation/lithiation process of the orthorhombic Nb_2O_5[45, 46]. The EPC structured Nb_2O_5/C nanohybrid and coral Nb_2O_5 present three redox pairs at 2.2 V/2.0 V, 1.8 V/1.6 V and 1.25 V/1.17 V, which are assigned to the lithium ion de-intercalation/intercalation process of the monoclinic Nb_2O_5. In addition, a small peak appears at 1.0 V - 1.2 V in the first cycle, indicating the formation of solid electrolyte interphase (SEI)[47].

Charge and discharge profiles of the CO_2 activated Nb_2O_5/C nanohybrids are displayed with a voltage range of 0.01 V – 3.0 V at a current density of 40 mA g^{-1} (**Figure 6b** and **Figure S5**). Apart from a small sloping plateau originated from the SEI formation process, no obvious plateau is observed in the first discharging cycle of the pristine carbon embedding Nb_2O_5/C nanohybrid (**Figure S5a**). After the CO_2 activation at 800 ˚C with an enhanced crystallization, a small plateau appears at 1.5 V on discharge and 1.8 V on charge, consistent with the CV results (**Figure S5b**). When the activation temperature increases to 900 ˚C, multiple plateaus between 1.0 V and 2.0 V are shown in the EPC structured Nb_2O_5/C nanohybrid and coral Nb_2O_5 samples (**Figure 6b** and **Figure S5c**). The main plateau at 1.6 V refers the sharp redox pair at 1.8 V/1.6 V in the CV profiles, which further confirms the charge/discharge behaviors of the monoclinic Nb_2O_5. The pristine carbon embedding Nb_2O_5/C, EDC structured Nb_2O_5/C, EPC structured Nb_2O_5/C and coral Nb_2O_5 deliver initial discharge/charge capacities of 535

mAh g^{-1}/192 mAh g^{-1}, 689 mAh g^{-1}/274 mAh g^{-1}, 750 mAh g^{-1}/396 mAh g^{-1} and 468 mAh g^{-1}/345 mAh g^{-1}, corresponding to initial coulombic efficiencies (ICE) of 35.9 %, 39.8 %, 52.8 % and 73.7 %, respectively. The large irreversible capacity is ascribed to intrinsic properties of resin-induced hard carbon and the formation of SEI on the surface of carbon matrix[47]. Thus, the ICE is improved after CO_2 activation process due to decreased carbon content.

Cycling performance of the Nb_2O_5/C nanohybrids is measured at a current density of 40 mA g^{-1} (**Figure 6c**). The EDC structured Nb_2O_5/C also present improved cycling performance than the pristine sample, while the coral Nb_2O_5 shows poor reversibility in 50 cycles. The total removal of the carbon matrix by the CO_2 activation deteriorates the overall electron conductivity of the electrode and lack of carbon matrix makes it difficult to buffer mechanical stress generated upon lithiation, which tends to accelerate capacity decay. The EPC structured Nb_2O_5/C shows the best performance, presenting a discharge capacity of 387 mAh g^{-1} after 200 cycles, which is nearly twice higher than the pristine and other activated samples. It is worth noting that the specific capacity of the EPC structured Nb_2O_5/C is much higher than the theoretical value of Nb_2O_5 (ca. 200 mAh g^{-1}), where the excessive lithium-ion storage is likely from the surface storage mechanism because of the increased surface area[48-50]. The CO_2 activated Nb_2O_5 nanohybrids present improved rate performance at various current densities of 0.1 C to 5 C, and reversed current density of 0.1 C (**Figure 6d**). The EPC structured Nb_2O_5 delivers a specific capacity of 169 mAh g^{-1} at 5 C, corresponding with capacity retention of 37.6 % with respect to the capacity at 0.1 C. In order to further investigate the cycling

and rate performance, correlative measurements are conducted at voltage window of 1.0 V - 3.0 V. **Figure 6e** shows that the EPC structured Nb_2O_5 remain a specific capacity of 184 mAh g^{-1} after 200 cycles, which retains 88 % of the initial capacity. The specific capacity is nearly 5 times higher than that of the pristine carbon embedding Nb_2O_5 (42 mAh g^{-1} after 40 cycles). The improved electrochemical performance at a reduced voltage window is due to enhanced crystallization of the Nb_2O_5 nanoparticles by CO_2 activation. Regarding the rate performance, the EPC structured Nb_2O_5 present capacity retention of 99 %, 93 %, 89 %, 79 % and 62 % at current density of 0.2 C, 0.5 C, 1 C, 2 C, and 5 C (**Figure 6f**). It is noted that coral Nb_2O_5 could not delivers comparable performances with the EPC structured Nb_2O_5 even coated with effective carbon matrix (**Figure S6**), illustrating superior ion transportation in EPC structure than conventional carbon coating. **Figure 6g** demonstrates the cycling stability of the EPC structured Nb_2O_5, delivering a capacity of 173 mAh g^{-1} after 500 cycles at 1 C. Both the cycling and rate performance of the Nb_2O_5/C nanohybrid is significantly improved by the emcoating technique, and to the best of our knowledge, the cycling performance of the EPC structured Nb_2O_5 is superior to the reported work at both cut-off voltages range of 0.01 V-3 V and 1.0 V – 3.0 V (**Table 2**).

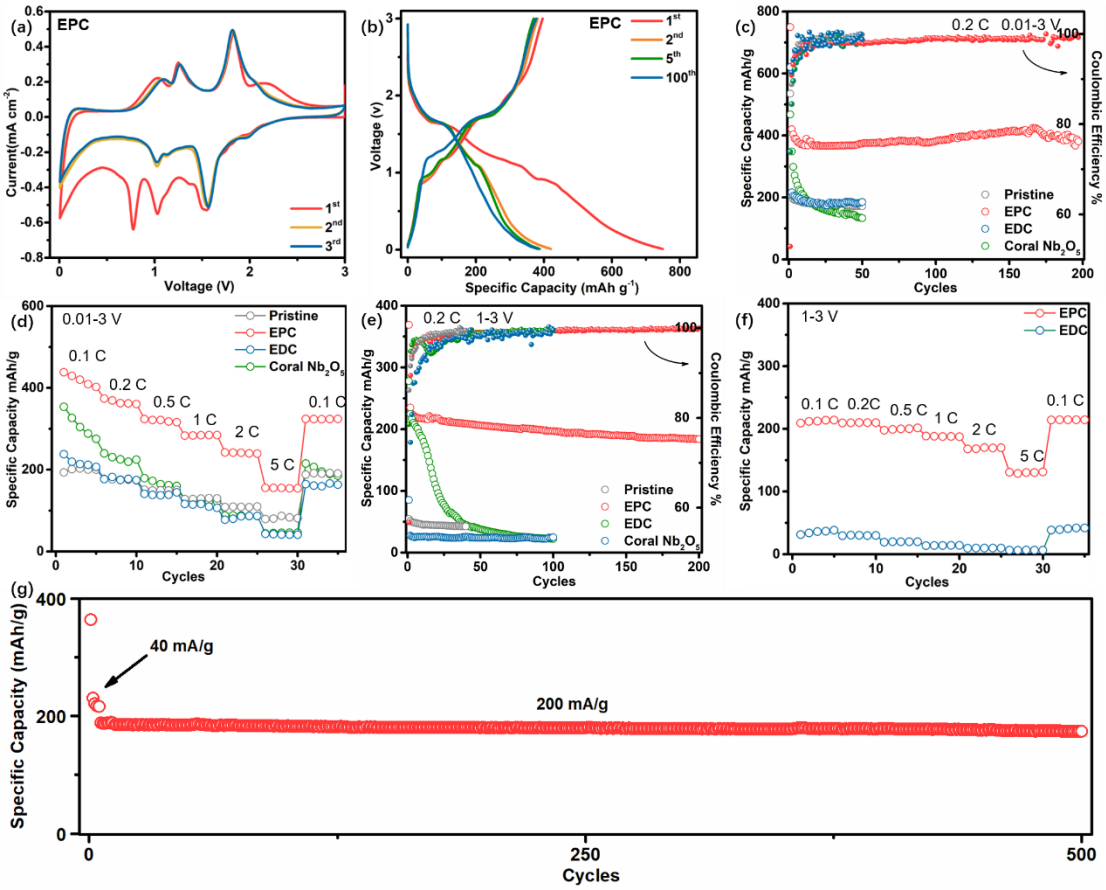

Figure 6. Electrochemical performance of the pristine carbon embedding Nb_2O_5/C and carbon emcoating Nb_2O_5/C (1 C=200 mA g^{-1}): charge/discharge profiles (a) and CV curves (b) of the EPC structured Nb_2O_5/C; cycling (c) and rate (d) performances of the pristine carbon embedding Nb_2O_5/C and carbon emcoating Nb_2O_5/C with the voltage range of 0.01 V - 3.0 V; cycling (e), rate (f), and long cycling performance at 200 mA g^{-1} (g) with the cut-off voltage from 1.0 V to 3.0 V.

Table 2. Electrochemical performance of the reported Nb_2O_5-based negative electrodes.

Electrode	Potential Range/V	Gravimetric Capacity/mAh g^{-1}	Current Density/mA g^{-1}	Ref.
NbO_2/C	0.01-3.0	225 (500^{th})	200	[[18]]
NbO_x@C	0.01-3.0	298 (100^{th})	100	[[51]]
Nb_2O_5/C	0.01-3.0	385 (100^{th})	100	[[52]]
Nb_2O_5 capsule	0-3	421 (100^{th})	100	[[53]]
Vein-like Nb_2O_5	1.0-3.0	201 (50^{th})	200	[[54]]
Nb_2O_5/CNTS	1.0-3.0	168 (500^{th})	100	[[53]]
Nb_2O_5/NbO_2	1.0-3.0	123 (900^{th})	200	[[55]]
Nb_2O_5	1.2-3.0	140 (200^{th})	100	[[56]]
Nb_2O_5/C	0.01-3.0 1.0-3.0	387 (200^{th}) 184 (500^{th})	40 200	This work

To reveal the mechanism governing the high rate performance of the EPC structured Nb_2O_5, kinetic related tests are carried out to determine the specific capacity contributions from the diffusion-controlled and capacitive processes[57]. **Figure 7a** presents the CV measurements of the EPC structured Nb_2O_5 and pristine carbon embedding sample with scan rates from 0.2 mV s^{-1} to 1.2 mV s^{-1} and the strong redox peak pair at 1.5 V refers to the de-lithiation/lithiation of Nb_2O_5. With increasing scan rates, the redox peaks tend to be broad and shift to high voltage due to polarization. The cathodic peak is marked as Peak 1, representing the lithium insertion process. According to Randles Sevcik equation, the peak current (I_p, A) from the CV scans can be applied to estimate the lithium diffusion coefficient of D_{Li}^+ (cm^2 s^{-1})[58]:

$$I_p = 2.69 \times 10^5 n^{3/2} A D^{1/2} v^{1/2} C \quad (3)$$

According to Randles Sevcik equation, the lithium diffusion coefficient of D_{Li}^+ of the EPC structured Nb_2O_5 and pristine carbon embedding Nb_2O_5 are estimated as $4.3 \times 10^{-11} \mathrm{cm}^2 s^{-1}$ and $7.4 \times 10^{-13} \mathrm{cm}^2 s^{-1}$, **Figure S7.**

In addition, the contribution of the capacitance process can be analyzed by the equation below:

$$i = a\nu^{b} \quad (4)$$

where i stands for the peak current, a and b are adjustable constants[59, 60]. The a and b values are empirical parameters, which can be calculated by fitting the $\log(\nu)$-$\log(i)$ plot (**Figure 7b**). Note that the b value indicates the contribution of diffusion controlled process and surface capacitance process. When the b value is close to 1, it represents a surface-controlled intercalation process. While the b value is close to 0.5, a diffusion-controlled process is dominating[59]. From the slope of $\log(\nu)$-$\log(i)$, the b values of cathodic (peak 1) and anodic (peak 2) are 0.68 and 0.78 respectively, which illustrates a surface-controlled process of the EPC structured Nb_2O_5/C. In addition, the contribution of the diffusion process and capacitance process can be extracted from the following equation:

$$i = k_1\nu + k_2\nu^{1/2} \quad (5)$$

where $k_1\nu$ stands for the contribution of the surface capacitance and $k_2\nu^{1/2}$ stands for the contribution of the diffusion-controlled process. **Figure 7c** and **7d** depicts that the proportion of capacitance contribution is 48.6 % at the scan rate of 0.2 mV s^{-1}. With increasing scan rates to 1.2 mV s^{-1}, the proportion rises to 70.0 %. Thus, the majority of the lithium storage of the EPC structured Nb_2O_5 originates from the capacitive behavior, which conduces to the excellent high rate performance.

GITT experiment is applied to investigate the lithium ion diffusion coefficient of the EPC structured Nb_2O_5. The cell is cycled at 0.1 C to reach stabilized cycling

performances before mesurement. **Figure 7e** shows the data for the GITT analysis during the discharge/charge process. The apparent D_{Li}^{+} can be estimated based on the equation derived from Fick's second law[61-63]:

$$D_{Li} = \frac{4}{\pi}\left(\frac{m_B V_m}{M_B S}\right)^2 \left(\frac{\Delta E_S}{\tau(dE_\tau/d\sqrt{\tau})}\right)^2, \tau \ll \frac{L^2}{D_{Li}} \quad (6)$$

Where m_B, M_B and V_m are the real mass, molar mass and molar volume of active material, respectively. S is area of the electrode and τ is the current pulse time. ΔE_τ is the potential change caused by pulse current in a single-step GITT experiment and ΔE_s is transient potential change after eliminating the IR drop, which can be extracted from **Figure 7f**. From **Figure 7g**, it can be extracted that E and $\tau^{1/2}$ present linear relationship during single titration. Thus, the equation 6 can be simplified as follow[61-63]:

$$D_{Li} = \frac{4}{\pi\tau}\left(\frac{m_B V_m}{M_B S}\right)^2 \left(\frac{\Delta E_S}{\Delta E_\tau}\right)^2, \ (\tau \ll \frac{L^2}{D_{Li}}) \quad (7)$$

D_{Li+} of the EPC structured Nb_2O_5/C during de-lithiation/lithiation process is calculated ranging from 10^{-10} cm^2s^{-1} to 10^{-18} cm^2s^{-1} (**Figure 7h**). The lithium diffusion coefficient calculated from GITT match well with the results from the CV analysis, which further confirms the rapid lithium ion diffusion behavior of the EPC structured Nb_2O_5/C nanohybrid.

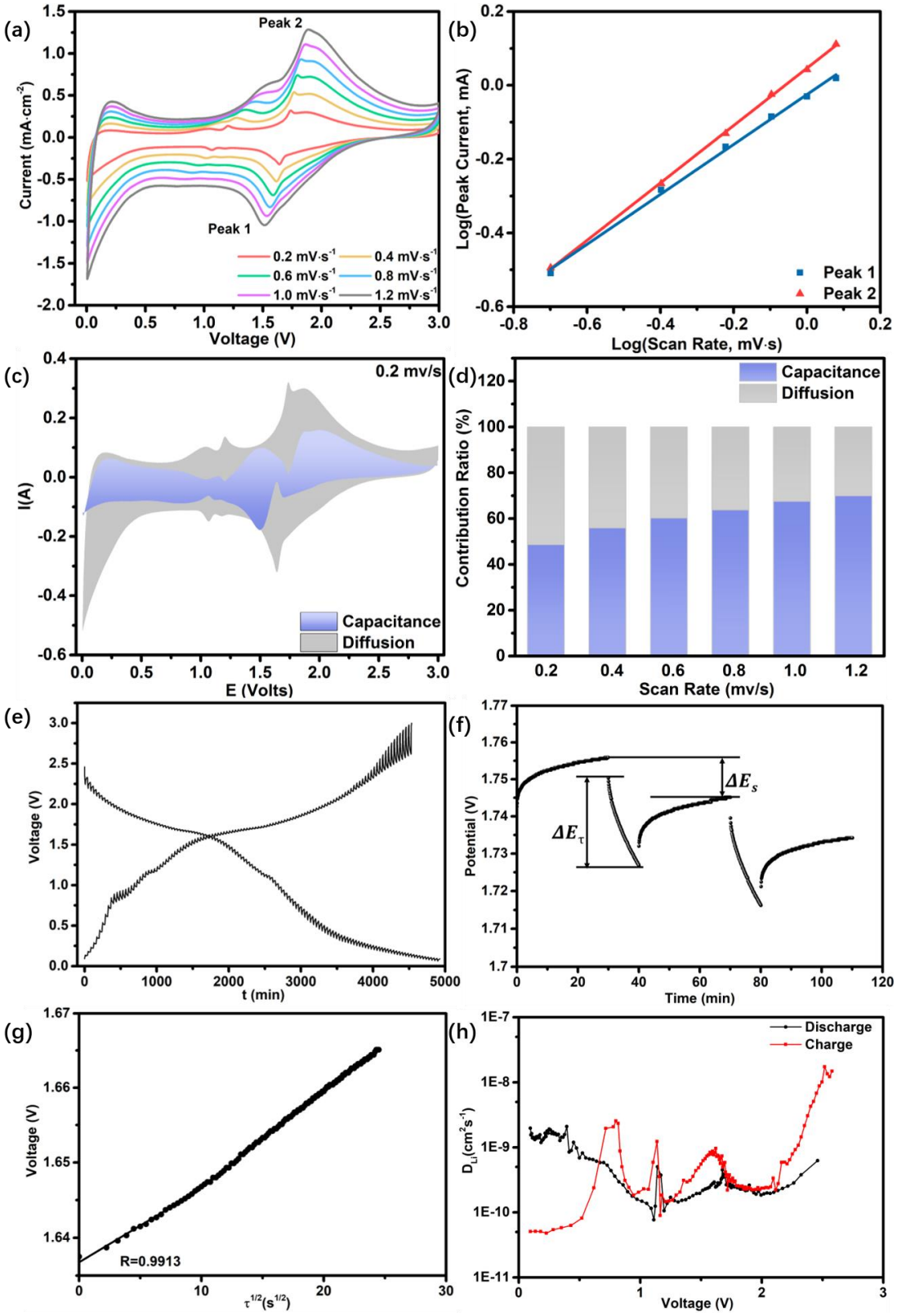

Figure 7. Kinetics analysis of the lithium ion storage mechanism of the EPC structured Nb_2O_5/C. Details: CV profiles at various scan rates (a); relationship between the peak current and scan rate in logarithmic format (b); capacitive contribution at scan rate of

0.2 mv s^{-1} (c); contribution ratio of the capacitive and diffusion-controlled capacities at various scan rates (d). GITT analysis of the EPC structured Nb_2O_5. Details: GITT profiles of the discharge/charge process (e); single step of the GITT curves (f); Linear fit of E versus $\tau^{1/2}$ for a typical titration (g); apparent lithium diffusion coefficient (D_{Li}) of the EPC structured Nb_2O_5/C calculated from the GITT profiles (h). Additionally, the electrochemical impedance spectra (EIS) results (**Figure S8**) confirm the improved diffusion behavior from the unique carbon structure as well.

The improved electrochemical performance of the EPC structured Nb_2O_5 is attributed to unique structure from the effect of CO_2 activation process. The crystal phase of the Nb_2O_5 component is modified and crystallization is also enhanced. With increasing crystallinity, lithiation plateau is prolonged. Besides, the bulk structure is tuned from embedding to interconnected and mesoporous carbon emcoating structure after CO_2 activation, the contact area between electrolyte and electrode is increased and the diffusion path is largely shortened, which facilitates the electron and ion transport. Compared with conventional coating structure, the interconnected carbon matrix provides more carbon composition on the surface of the Nb_2O_5 nanoparticles. In addition, re-constructed surface and increase of surface area enhances lithium-ion storage capability due to additional surface lithium storage process for the CO_2 activated Nb_2O_5/C nanohybrids.

The intercalation negative electrode is implicated with gassing problems, which hampers the practical application[64, 65]. The gassing behavior of the EPC structured Nb_2O_5 electrode is explored with differential electrochemical mass spectrometry (DEMS) (**Figure 8a**). Gas species with molecular weight of 44, 30, 28, and 2 were monitored to characterize CO_2, C_2H_6, C_2H_4 and H_2, respectively. Commercial lithium titanate (LTO) is applied as the control sample (**Figure 8b**). The gas evolution profiles for the first galvanostatic discharge/charge cycles at 0.1 C are presented. During the discharge process, different from LTO, gas evolution of C_2H_4 and C_2H_6 is observed, which could be attributed to the reduction of EC and DMC[64, 66, 67]. The origination of H_2 during discharge is assigned to the reduction of trace water from electrode[68]. Nevertheless, as the feature gas of the LTO electrode from reduction of Ti^{4+} to Ti^{3+}, CO_2 is only observed in the LTO electrode[69]. After integration, the specific gas amount of the EPC structured Nb_2O_5/C nanohybrid and LTO are calculated as 2.47 μmol and 3.04 μmol, implying that the EPC structured Nb_2O_5/C nanohybrid exhibits a reduced gas evolution behavior than the commercial LTO electrode.

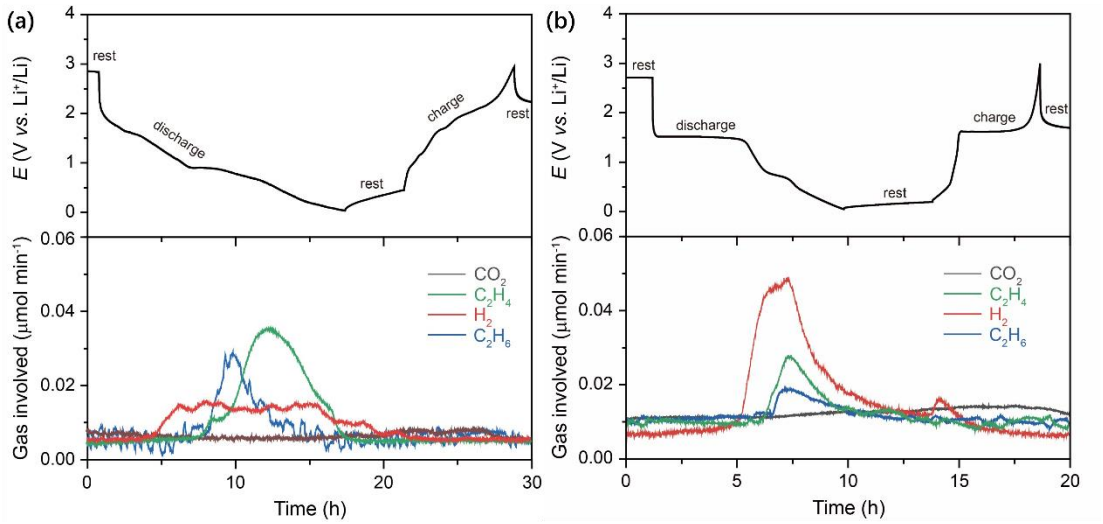

Figure 8. DEMS patterns with initial discharge/charge cycle of the EPC structured Nb_2O_5/C (a) and commercial LTO electrode (b).

CONCLUSIONS

In summary, Nb_2O_5/C nanohybrid with the carbon-emcoating architecture is constructed through CO_2 activation treatment of the Nb_2O_5/C sample with the Nb_2O_5 nanoparticles embedded in the carbon matrix. Triple structure engineering of the carbon-emcoated Nb_2O_5/C nanohybrid is achieved by the CO_2 activation process, where the content and microstructure of the carbon matrix, and crystallographic phase of the Nb_2O_5 are well tuned. Compared to the typical carbon-coating and carbon-embedding structure, dominant interior surface of the Nb_2O_5 nanoparticulate agglomerate is covered by the continuous porous carbon within the carbon-emcoated Nb_2O_5/C nanohybrid. Superior electrochemical performance is exhibited by the EPC structured Nb_2O_5/C nanohybrid: a discharging capacity of 387 mAh g^{-1} over 200 cycles is demonstrated. With the narrowed voltage window of 1.0-3.0 V, a capacity of 173 mAh $g^{-`1}$ is maintained after 500 cycles. The D_{Li^+} of the EPC structured Nb_2O_5/C nanohybrid shows two order of magnitude higher than non-activated samples. The DEMS profile indicates that the EPC structured Nb_2O_5/C nanohybrid exhibits reduced gassing behavior compared to the commercial lithium titanate counterpart. The work presented in this manuscript provides a facile method and fundamental understanding about construction of the carbon-emcoating architecture towards high performance energy storage materials.

EXPERIMENTAL SECTION

Materials

Niobium (V) Ethoxide (NbETO) was purchased from Alfa Aesar (China) Co., Ltd. Bisphenol A-glycidyl methacrylate (Bis-GMA) and tert-Butyl peroxy benzoate (TBPB) were obtained from Sigma-Aldrich. Poly (vinylidene fluoride) (PVDF) was donated by Solvay. Conductive carbon black (Super P) was purchased from SCM Chem. Shanghai, China. N-methyl pyrrolidone (NMP) was acquired from Aladdin Reagent Co., Ltd, China. All chemicals were used as received.

Sample Preparation

The pristine embedding type Nb_2O_5/C nanohybrids were prepared according to our previous work with the Bis-GMA/NbETO mass ratio of 1:1[18]. The carbon emcoating samples were prepared with further heat treatment at 900 ˚C under CO_2 atmosphere with a flow rate of 0.5 L min^{-1} for 1 hour. To study the mechanism responsible for the structure evolution during CO_2 heat treatment, the pristine samples were treated by CO_2 at 900 ˚C for 2 h and 800 ˚C for 1h and 2 h as well.

Material Characterization

X-Ray diffractometer (XRD; Bruker AXS D8 Advance, λ=1.5406 Å, 2.2 kW) was applied to identify the crystallographic phases of the niobium oxide/carbon nanohybrids and CO_2 activated samples with 2θ from 5 ° to 90 °. X-ray photoelectron spectroscopy (XPS) measurements were characterized on an ESCALAB 250 XI model spectrometer with Al Kα radiation (hν= 1486.6 eV). Scanning electron microscope (SEM; Hitachi S4800) was used to characterize the morphology at an accelerating voltage of 4 kV. The

carbon content was measured by a Mettler Toledo thermos-gravimetric analyzer (TGA) with a temperature range from 50 ˚C to 800 ˚C at a ramp rate of 20 ˚C min^{-1} in air. Phase structure of the niobium oxide/carbon nanohybrids was determined by Raman Spectroscopy (Renishaw, in Via-reflex). A JEOL JEM-2100F transmission electron microscopy (TEM) was adopted for high-resolution imaging and selected area electron diffraction (SAED). Specimens for TEM were prepared by sonicating the Nb_2O_5/C powders in ethanol for 10 minutes, which were then dropped onto a cooper grid and dried by an infrared lamp. A Micromeritics ASAP2020 was applied to characterize the Brunauer-Emmett-Teller (BET) surface area and pore size distribution profile with N_2 adsorption isotherms at 77 K.

Electrochemical Measurement

The electrochemical performance was evaluated using CR-2032 type coin cells in a half-cell configuration. Electrodes were prepared by manual mixing of the nanohybrid material, super P and PVDF in a mortar with a mass ratio of 8:1:1, where NMP was used as the dispersion medium. The mixture was then cast onto copper foil and dried at 80 ˚C for 4 h. Typical electrode presents a mass density between 2 mg cm^{-2} and 3 mg cm^{-2}. Coin cells were assembled with lithium metal foil (Dongguan Shanshan battery Materials Co., LTD) and Celgard 2400 microporous polypropylene membrane as counter electrode and separator, respectively, in Argon-filled glove box. Electrolyte from Zhangjiagang Guotai-Huarong Commercial New Material Co., LTD was adopted, with 1.0 M $LiPF_6$ dissolved in a solution mixture of ethylene carbonate (EC), dimethyl carbonate (DMC) and fluoroethylene carbonate (EC: DMC=1:1 by volume, FEC 5 %

by mass). A Neware Battery Test System was employed to conduct galvanostatic cycling and rate tests at a voltage range from 0.01 V to 3.0 V (versus Li^+/Li) and from 1.0 V to 3.0 V (versus Li^+/Li). 1 C current rate is set as 200 mA g^{-1}. A Solartron Analytical electrochemical workstation was used for cyclic voltammetry (CV, 0.001 V-3.0 V, 0.2 mV s^{-1}) and electrochemical impedance spectroscopy (EIS, 0.001 HZ – 1 MHz, 10 mv) measurements. The galvanostatic intermittent titration technique (GITT) test was carried out on Neware Battery Test System. The battery was discharged and charged with a small pulse current at 20 mA g^{-1} for 10 min followed by a rest period of 30 min at a potential from 0.01 V to 3.0 V.

Differential electrochemical mass spectrometry (DEMS) was conducted according to previously reported work[64, 70, 71]. Measurements was conducted with Swagelok type cell. Argon with a flow rate of 0.5 ml min^{-1} was applied as conveying gas to flush out the gas generated.

REFERENCES

1 Ohzuku T, Ueda A, Yamamoto N. Zero-Strain Insertion Material of $Li[Li_{1/3}Ti_{5/3}]O_4$ for Rechargeable Lithium Cells. J Electrochem Soc. 1995, 142: 1431-1435

2 Poizot P, Laruelle S, Grugeon S, Dupont L, Tarascon JM. Nano-sized transition-metal oxides as negative-electrode materials for lithium-ion batteries. Nature. 2000, 407: 496-499

3 Hu Y-S, Kienle L, Guo Y-G, Maier J. High Lithium Electroactivity of Nanometer-Sized Rutile TiO_2. Adv Mater. 2006, 18: 1421-1426

4 Zhao Y, Wang LP, Sougrati MT, Feng Z, Leconte Y, Fisher A, Srinivasan M, Xu Z. A Review on Design Strategies for Carbon Based Metal Oxides and Sulfides Nanocomposites for High Performance Li and Na Ion Battery Anodes. Adv Energy Mater. 2017, 7: 1601424

5 Kim K-T, Yu C-Y, Yoon CS, Kim S-J, Sun Y-K, Myung S-T. Carbon-coated $Li_4Ti_5O_{12}$ nanowires showing high rate capability as an anode material for rechargeable sodium batteries. Nano Energy. 2015, 12: 725-734

6 Li N, Zhou G, Li F, Wen L, Cheng H-M. A Self-Standing and Flexible Electrode of $Li_4Ti_5O_{12}$ Nanosheets with a N-Doped Carbon Coating for High Rate Lithium Ion Batteries. Adv Funct Mater. 2013, 23: 5429-5435

7 Zhu G-N, Liu H-J, Zhuang J-H, Wang C-X, Wang Y-G, Xia Y-Y. Carbon-coated nano-sized $Li_4Ti_5O_{12}$ nanoporous micro-sphere as anode material for high-rate lithium-ion batteries. Energy Environ Sci. 2011, 4: 4016-4022

8 Ko YN, Park SB, Jung KY, Kang YC. One-Pot Facile Synthesis of Ant-Cave-Structured Metal Oxide–Carbon Microballs by Continuous Process for Use as Anode Materials in Li-Ion Batteries. Nano Lett. 2013, 13: 5462-5466

9 Li W, Wang F, Feng S, Wang J, Sun Z, Li B, Li Y, Yang J, Elzatahry AA, Xia Y, Zhao D. Sol–Gel Design Strategy for Ultradispersed TiO_2 Nanoparticles on Graphene for High-Performance Lithium Ion Batteries. J Am Chem Soc. 2013, 135: 18300-18303

10 Liu Y, Zhang N, Jiao L, Tao Z, Chen J. Ultrasmall Sn Nanoparticles Embedded in Carbon as High-Performance Anode for Sodium-Ion Batteries. Adv Funct Mater. 2015, 25: 214-220

11 Chen Z, Dahn JR. Reducing Carbon in $LiFePO_4$/C Composite Electrodes to Maximize Specific Energy, Volumetric Energy, and Tap Density. J Electrochem Soc. 2002, 149: A1184-A1189

12 Ko YN, Kang YC. Co_9S_8–carbon composite as anode materials with improved Na-storage performance. Carbon. 2015, 94: 85-90

13 Lu Y, Zhang N, Zhao Q, Liang J, Chen J. Micro-nanostructured CuO/C spheres as high-performance anode materials for Na-ion batteries. Nanoscale. 2015, 7: 2770-2776

14 Zhang N, Han X, Liu Y, Hu X, Zhao Q, Chen J. 3D Porous γ-Fe_2O_3@C Nanocomposite as High-Performance Anode Material of Na-Ion Batteries. Adv Energy Mater. 2015, 5: 1401123

15 Xiao Y, Wang X, Xia Y, Yao Y, Metwalli E, Zhang Q, Liu R, Qiu B, Rasool M, Liu Z. Green Facile Scalable Synthesis of Titania/Carbon Nanocomposites: New Use of Old Dental Resins. ACS Appl Mater Interfaces. 2014, 6: 18461-18468

16 Wang X, Meng JQ, Wang M, Xiao Y, Liu R, Xia Y, Yao Y, Metwalli E, Zhang Q, Qiu B, Liu Z, Pan J, Sun LD, Yan CH, Muller-Buschbaum P, Cheng YJ. Facile Scalable Synthesis of TiO_2/Carbon Nanohybrids with Ultrasmall TiO_2 Nanoparticles Homogeneously Embedded in Carbon Matrix. ACS Appl Mater Interfaces. 2015, 7: 24247-24255

17 Zheng L, Wang X, Xia Y, Xia S, Metwalli E, Qiu B, Ji Q, Yin S, Xie S, Fang K, Liang S, Wang M, Zuo X,

Xiao Y, Liu Z, Zhu J, Müller-Buschbaum P, Cheng Y-J. Scalable in Situ Synthesis of $Li_4Ti_5O_{12}$/Carbon Nanohybrid with Supersmall $Li_4Ti_5O_{12}$ Nanoparticles Homogeneously Embedded in Carbon Matrix. ACS Appl Mater Interfaces. 2018, 10: 2591-2602

18 Ji Q, Gao X, Zhang Q, Jin L, Wang D, Xia Y, Yin S, Xia S, Hohn N, Zuo X, Wang X, Xie S, Xu Z, Ma L, Chen L, Chen GZ, Zhu J, Hu B, Müller-Buschbaum P, Bruce PG, Cheng Y-J. Dental Resin Monomer Enables Unique NbO_2/Carbon Lithium-Ion Battery Negative Electrode with Exceptional Performance. Adv Funct Mater. 2019, 29: 1904961

19 Wang X, Ma L, Ji Q, Meng J-Q, Liang S, Xu Z, Wang M, Zuo X, Xiao Y, Zhu J, Xia Y, Müller-Buschbaum P, Cheng Y-J. MnO/Metal/Carbon Nanohybrid Lithium-Ion Battery Anode With Enhanced Electrochemical Performance: Universal Facile Scalable Synthesis and Fundamental Understanding. Adv Mater Interfaces. 2019, 6: 1900335

20 Yang Z, Shen J, Archer LA. An in situ method of creating metal oxide–carbon composites and their application as anode materials for lithium-ion batteries. J Mater Chem. 2011, 21: 11092

21 Chen Y, Ma X, Cui X, Jiang Z. In situ synthesis of carbon incorporated TiO_2 with long-term performance as anode for lithium-ion batteries. J Power Sources. 2016, 302: 233-239

22 Cao S, Feng X, Song Y, Liu H, Miao M, Fang J, Shi L. In Situ Carbonized Cellulose-Based Hybrid Film as Flexible Paper Anode for Lithium-Ion Batteries. ACS Appl Mater Interfaces. 2016, 8: 1073-1079

23 Ryu SK, Jin H, Gondy D, Pusset N, Ehrburger P. Activation of carbon fibres by steam and carbon dioxide. Carbon. 1993, 31: 841-842

24 Rodríguez-Reinoso F, Molina-Sabio M, González MT. The use of steam and CO_2 as activating agents in the preparation of activated carbons. Carbon. 1995, 33: 15-23

25 Xia K, Gao Q, Wu C, Song S, Ruan M. Activation, characterization and hydrogen storage properties of the mesoporous carbon CMK-3. Carbon. 2007, 45: 1989-1996

26 Xia K, Gao Q, Jiang J, Hu J. Hierarchical porous carbons with controlled micropores and mesopores for supercapacitor electrode materials. Carbon. 2008, 46: 1718-1726

27 Xia K, Gao Q, Song S, Wu C, Jiang J, Hu J, Gao L. CO_2 activation of ordered porous carbon CMK-1 for hydrogen storage. Int J Hydrog Energy. 2008, 33: 116-123

28 Sevilla M, Mokaya R. Energy storage applications of activated carbons: supercapacitors and hydrogen storage. Energy Environ Sci. 2014, 7: 1250-1280

29 Zhang Y, Park S-J. Incorporation of RuO_2 into charcoal-derived carbon with controllable microporosity by CO_2 activation for high-performance supercapacitor. Carbon. 2017, 122: 287-297

30 Roh J-S. Structural study of the activated carbon fiber using laser Raman spectroscopy. Carbon Lett. 2008, 9: 127-130

31 Balachandran U, Eror NG. Raman spectrum of the high temperature form of Nb_2O_5. J Mater Sci Lett. 1982, 1: 374-376

32 Schrader B, Bergmann G. Die Intensität des Ramanspektrums polykristalliner Substanzen. Anal Chem. 1967, 225: 230-247

33 Zhu S, Li J, Ma L, Guo L, Li Q, He C, Liu E, He F, Shi C, Zhao N. Three-Dimensional Network of N-Doped Carbon Ultrathin Nanosheets with Closely Packed Mesopores: Controllable Synthesis and Application in Electrochemical Energy Storage. ACS Appl Mater Interfaces. 2016, 8: 11720-11728

34 Hubbard CR, Snyder RL. RIR - Measurement and Use in Quantitative XRD. Powder Diffr. 2013, 3: 74-77

35 Li Y, Zhang S, Yu Q, Yin W. The effects of activated carbon supports on the structure and properties of TiO_2 nanoparticles prepared by a sol–gel method. Appl Surf Sci. 2007, 253: 9254-9258

36 Li Q, Liu B, Li Y, Liu R, Li X, Li D, Yu S, Liu D, Wang P, Li B, Zou B, Cui T, Zou G. Ethylene glycol-mediated synthesis of nanoporous anatase TiO_2 rods and rutile TiO_2 self-assembly chrysanthemums. J Alloy Compd. 2009, 471: 477-480

37 Bailón-García E, Elmouwahidi A, Álvarez MA, Carrasco-Marín F, Pérez-Cadenas AF, Maldonado-Hódar FJ. New carbon xerogel-TiO_2 composites with high performance as visible-light photocatalysts for dye mineralization. Appl Catal B. 2017, 201: 29-40

38 Du X, Wu Y, Kou Y, Mu J, Yang Z, Hu X, Teng F. Amorphous carbon inhibited TiO_2 phase transition in aqueous solution and its application in photocatalytic degradation of organic dye. J Alloy Compd. 2019, 810: 151917

39 Xiao Q, Zhang J, Xiao C, Si Z, Tan X. Solar photocatalytic degradation of methylene blue in carbon-doped TiO_2 nanoparticles suspension. Sol Energy. 2008, 82: 706-713

40 Ohno T, Tsubota T, Toyofuku M, Inaba R. Photocatalytic Activity of a TiO_2 Photocatalyst Doped with C^{4+} and S^{4+} Ions Having a Rutile Phase Under Visible Light. Catal Letters. 2004, 98: 255-258

41 Yabuuchi N, Yoshii K, Myung S-T, Nakai I, Komaba S. Detailed Studies of a High-Capacity Electrode Material for Rechargeable Batteries, Li_2MnO_3–$LiCo_{1/3}Ni_{1/3}Mn_{1/3}O_2$. J Am Chem Soc. 2011, 133: 4404-4419

42 Schäfer H, Gruehn R, Schulte F. Die Modifikationen des Niobpentoxids. Angew Chem Int Ed. 1966, 78: 28-41

43 Pilarek B, Pelczarska AJ, Szczygieł I. Characterization of niobium(v) oxide received from different sources. J Therm Anal Calorim. 2017, 130: 77-83

44 Valencia-Balvín C, Pérez-Walton S, Dalpian GM, Osorio-Guillén JM. First-principles equation of state and phase stability of niobium pentoxide. Comput Mater Sci. 2014, 81: 133-140

45 Viet AL, Reddy MV, Jose R, Chowdari BVR, Ramakrishna S. Nanostructured Nb_2O_5 Polymorphs by Electrospinning for Rechargeable Lithium Batteries. J Phys Chem C. 2010, 114: 664-671

46 Rahman MM, Rani RA, Sadek AZ, Zoolfakar AS, Field MR, Ramireddy T, Kalantar-Zadeh K, Chen Y. A vein-like nanoporous network of Nb_2O_5 with a higher lithium intercalation discharge cut-off voltage. J Mater Chem A. 2013, 1: 11019-11025

47 Flandrois S, Simon B. Carbon materials for lithium-ion rechargeable batteries. Carbon. 1999, 37: 165-180

48 Duan Y, Zhang B, Zheng J, Hu J, Wen J, Miller DJ, Yan P, Liu T, Guo H, Li W, Song X, Zhuo Z, Liu C, Tang H, Tan R, Chen Z, Ren Y, Lin Y, Yang W, Wang C-M, Wang L-W, Lu J, Amine K, Pan F. Excess Li-Ion Storage on Reconstructed Surfaces of Nanocrystals To Boost Battery Performance. Nano Lett. 2017, 17: 6018-6026

49 Shin J-Y, Samuelis D, Maier J. Sustained Lithium-Storage Performance of Hierarchical, Nanoporous Anatase TiO_2 at High Rates: Emphasis on Interfacial Storage Phenomena. Adv Funct Mater. 2011, 21: 3464-3472

50 Kumagai N, Koishikawa Y, Komaba S, Koshiba N. Thermodynamics and Kinetics of Lithium Intercalation into Nb_2O_5 Electrodes for a 2 V Rechargeable Lithium Battery. J Electrochem Soc. 1999, 146: 3203-3210

51 Cai Y, Li X, Wang L, Gao H, Zhao Y, Ma J. Oleylamine-assisted hydrothermal synthesis of ultrasmall NbOx nanoparticles and their in situ conversion to NbOx@C with highly reversible lithium storage. J Mater Chem A. 2015, 3: 1396-1399

52 Lin J, Yuan Y, Su Q, Pan A, Dinesh S, Peng C, Cao G, Liang S. Facile synthesis of Nb_2O_5/carbon nanocomposites as advanced anode materials for lithium-ion batteries. Electrochim Acta. 2018, 292:

63-71
53 Wu W, Huang J, Li J, Zhou L, Cao L, Cheng Y, He Y, Li Q. Inducing [001]-orientation in Nb_2O_5 capsule-nanostructure for promoted Li^+ diffusion process. Electrochim Acta. 2019, 298: 449-458
54 Rahman MM, Rani RA, Sadek AZ, Zoolfakar AS, Field MR, Ramireddy T, Kalantar-zadeh K, Chen Y. A vein-like nanoporous network of Nb_2O_5 with a higher lithium intercalation discharge cut-off voltage. J Mater Chem A. 2013, 1: 11019-11025
55 Park H, Lee D, Song T. High capacity monoclinic Nb_2O_5 and semiconducting NbO_2 composite as high-power anode material for Li-Ion batteries. J Power Sources. 2019, 414: 377-382
56 Cao D, Yao Z, Liu J, Zhang J, Li C. H-Nb_2O_5 wired by tetragonal tungsten bronze related domains as high-rate anode for Li-ion batteries. Energy Stor Mater. 2018, 11: 152-160
57 Chao D, Zhu C, Yang P, Xia X, Liu J, Wang J, Fan X, Savilov SV, Lin J, Fan HJ, Shen ZX. Array of nanosheets render ultrafast and high-capacity Na-ion storage by tunable pseudocapacitance. Nat Commun. 2016, 7: 12122
58 Dahn JR, Jiang J, Moshurchak LM, Fleischauer MD, Buhrmester C, Krause LJ. High-Rate Overcharge Protection of $LiFePO_4$-Based Li-Ion Cells Using the Redox Shuttle Additive 2,5-Ditertbutyl-1,4-dimethoxybenzene. J Electrochem Soc. 2005, 152: A1283-A1289
59 Lindström H, Södergren S, Solbrand A, Rensmo H, Hjelm J, Hagfeldt A, Lindquist S-E. Li^+ Ion Insertion in TiO_2 (Anatase). 2. Voltammetry on Nanoporous Films. J Phys Chem B. 1997, 101: 7717-7722
60 Augustyn V, Simon P, Dunn B. Pseudocapacitive oxide materials for high-rate electrochemical energy storage. Energy Environ Sci. 2014, 7: 1597-1614
61 Weppner W, Huggins RA. Determination of the Kinetic Parameters of Mixed - Conducting Electrodes and Application to the System Li_3Sb. J Electrochem Soc. 1977, 124: 1569-1578
62 Inada R, Kumasaka R, Inabe S, Tojo T, Sakurai Y. Li^+ Insertion/Extraction Properties for $TiNb_2O_7$ Single Particle Characterized by a Particle-Current Collector Integrated Microelectrode. J Electrochem Soc. 2019, 166: A5157-A5162
63 Rui XH, Ding N, Liu J, Li C, Chen CH. Analysis of the chemical diffusion coefficient of lithium ions in $Li_3V_2(PO_4)_3$ cathode material. Electrochim Acta. 2010, 55: 2384-2390
64 He M, Castel E, Laumann A, Nuspl G, Novák P, Berg EJ. In Situ Gas Analysis of $Li_4Ti_5O_{12}$ Based Electrodes at Elevated Temperatures. J Electrochem Soc. 2015, 162: A870-A876
65 Lanz M, Novák P. DEMS study of gas evolution at thick graphite electrodes for lithium-ion batteries: the effect of γ-butyrolactone. J Power Sources. 2001, 102: 277-282
66 Onuki M, Kinoshita S, Sakata Y, Yanagidate M, Otake Y, Ue M, Deguchi M. Identification of the Source of Evolved Gas in Li-Ion Batteries Using ^{13}C-labeled Solvents. J Electrochem Soc. 2008, 155: A794
67 He Y-B, Li B, Liu M, Zhang C, Lv W, Yang C, Li J, Du H, Zhang B, Yang Q-H, Kim J-K, Kang F. Gassing in $Li_4Ti_5O_{12}$-based batteries and its remedy. Sci Rep. 2012, 2: 913
68 Bernhard R, Meini S, Gasteiger HA. On-Line Electrochemical Mass Spectrometry Investigations on the Gassing Behavior of $Li_4Ti_5O_{12}$ Electrodes and Its Origins. J Electrochem Soc. 2014, 161: A497-A505
69 Fell CR, Sun L, Hallac PB, Metz B, Sisk B. Investigation of the Gas Generation in Lithium Titanate Anode Based Lithium Ion Batteries. J Electrochem Soc. 2015, 162: A1916-A1920
70 Gao X, Chen Y, Johnson L, Bruce PG. Promoting solution phase discharge in Li-O_2 batteries containing weakly solvating electrolyte solutions. Nat Mater. 2016, 15: 882-888
71 Chen Y, Freunberger SA, Peng Z, Bardé F, Bruce PG. Li–O_2 Battery with a Dimethylformamide Electrolyte. J Am Chem Soc. 2012, 134: 7952-7957

ACKNOWLEDGEMENT

The authors would like to thank Prof. Dr. Zhicheng Zhong and Dr. Ri He from Ningbo Institute of Materials Technology & Engineering, CAS for scientific discussions about phase conversion mechanism. The help from Prof. Dr. Qiuju Zhang in the Ningbo Institute of Materials Technology & Engineering, CAS, about structure modelling of Nb_2O_5 is appreciated. The authors also would like to thank Prof. Dr. Wei Cao from Ningbo University for scientific discussions about the emcoating structure interpretation. This research is funded by the National Key R&D Program of China (Grant No. 2016YFB0100100), the National Natural Science Foundation of China (51702335, 21773279), the Zhejiang Non-profit Technology Applied Research Program (LGG19B010001), Ningbo Municipal Natural Science Foundation (2018A610084), the CAS-EU S&T cooperation partner program (174433KYSB20150013), and Key Laboratory of Bio-based Polymeric Materials of Zhejiang Province. Y.-J. Cheng acknowledges funding by the Marie Sklodowska-Curie Fellowship from EU. P.G.B. is indebted to the Engineering and Physical Sciences Research Council (EPSRC), including the SUPERGEN Energy Storage Hub (EP/L019469/1), Enabling Next Generation Lithium Batteries (EP/M009521/1), Henry Royce Institute for Advanced Materials (EP/R00661X/1, EP/S019367/1, EP/R010145/1) and the Faraday Institution All-Solid-State Batteries with Li and Na Anodes (FIRG007, FIRG008) for financial support.

AUTHOR CONTRIBUTION

Cheng Y conceived the idea. Ji Q and Wang X designed the experiments and contributed to data analysis. Zuo X carried out TEM and RAMAN tests. Xu Z operated the

theoretical calculation and GITT measurements. Gao X designed and performed DEMS test. The paper was written by Ji Q with support from Cheng Y. All authors helped in the revision of the paper and contributed to the general discussion.

CONFLICTS OF INTEREST

The authors declare that they have no conflict of interest.

SUPPLEMENTARY INFORMATION

SEM, TEM, HRTEM, and SAED images of the coral Nb_2O_5 sample; thermogravimetric profiles and Raman spectroscopy of the pristine carbon embedding and CO_2-activated Nb_2O_5/carbon nanohybrids; carbon content and relative intensities of D band & G band of the Nb_2O_5/carbon nanohybrids prepared with different CO_2 activation conditions; BET surface area of the pristine and CO_2-activated Nb_2O_5/carbon nanohybrids at various conditions; XPS survey and high resolution of O1s, C1s and Nb3d of the pristine carbon embedding Nb_2O_5, EDC structured Nb_2O_5 and coral Nb_2O_5; peak area comparison of carbonate and C-C & carbonate and Nb-O; CV and discharge/charge profiles of the pristine, EDC structured Nb_2O_5 and coral Nb_2O_5; performance comparison of the EPC structured Nb_2O_5 and carbon coated Nb_2O_5; relationship between peak current (I_P) and the square root of scan rate ($v^{1/2}$) of the EPC structured Nb_2O_5. Supplementary data is available in the online version of the paper.

TABLE OF CONTENT

Unique carbon-emcoating structure with effective carbon coating on the dominant interior surface of the Nb_2O_5 nanoparticulate agglomerate is fabricated by a single CO_2 activation treatment of the carbon-embedding Nb_2O_5/C nanohybrid, accompanied with

a simultaneous triple structure engineering of the carbon-emcoated Nb_2O_5/C nanohybrid, where excellent long cycling life and rate performance are demonstrated compared to the conventional carbon coating and carbon embedding samples.

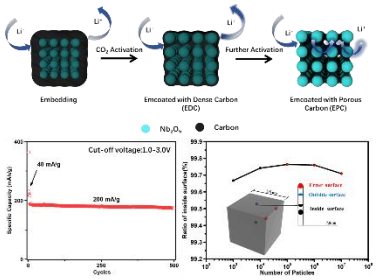

Qing Ji received his BE degree from Beijing University of Chemical Technology (2012). He is a PhD candidate at the University of Nottingham Ningbo China, jointly with Ningbo Institute of Materials Technology and Engineering, CAS. His research interest covers negative electrodes for lithium-ion batteries.

Ya-Jun Cheng is currently a professor in Ningbo Institute of Materials Technology and Engineering, Chinese Academy of Sciences. He received a B.S. degree from Peking University, China, followed by a Master degree from the University of Siegen, Germany, and completed Ph.D. studies at the Max-Planck Institute for Polymer Research in Mainz, Germany. His research interests focus on polymer/inorganic nanohybrids for advanced battery applications.

Binjie Hu received her PhD degree at the University of Newcastle, UK. Then she worked as research fellow and teaching fellow in the University of Birmingham, UK (2000-2006) and University of Cambridge, UK (2007-2010), respectively. She is currently an associate professor of University of Nottingham Ningbo China. Her research areas cover micro/nano-materials engineering and green engineering.

Yonggao Xia received his Ph.D. in energy and materials science from Saga University, Japan (2008). He is currently a professor in the Ningbo Institute of Materials Technology and Engineering, Chinese Academy of Sciences, heading the research group of Novel Organic Electrolyte and Corresponding Devices. His research covers advanced materials and technologies for lithium-ion batteries.

通过构筑嵌覆型碳结构提升 Nb_2O_5 储锂性能

姬青[1,2†]，徐佳军[1,3†]，杲祥文[4,5†]，程亚军[1,4*]，王晓艳[1]，左秀霞[1]，陈政[2,6]，胡斌杰[2*]，朱锦[1]，Peter G. Bruce[4,7,8]，夏永高[1,9]

摘要　嵌入型过渡金属氧化物因具有安全的工作电压，高比容量和快速的嵌锂能力而受到广泛的关注。但低本征电导率的特性严重影响其作为锂电负极材料的寿命和性能。本文通过简便易行、可规模化放大的二氧化碳热处理方法构筑具有新型嵌覆型碳结构的 Nb_2O_5/C 纳米杂化材料。在控制碳含量前提下，实现颗粒聚集体内部表面可控碳包覆。以嵌覆型碳结构的 Nb_2O_5/C 纳米杂化材料为负极组装的锂离子电池在 40 mA g^{-1} 电流密度下容量可达 387 mAh g^{-1}，而在 200 mA g^{-1} 电流密度下循环 500 周后，容量保持率在 92%以上。采用电化学滴定、差分电化学质谱（DEMS）等方法对嵌覆型五氧化二铌/碳纳米杂化材料脱嵌锂动力学过程以及产气行为进行了研究。本文提出的嵌覆型碳结构有望为高性能嵌入型过渡金属氧化物结构设计提供参考。